

The effect of overlying tissue on the spatial sensitivity profile of near-infrared spectroscopy

Eiji Okada†, Michael Firbank and David T Delpy

Department of Medical Physics and Bioengineering, University College London, 1st Floor, Shropshire House, 11–20 Capper Street, London WC1E 6JA, UK

Received 22 May 1995, in final form 24 August 1995

Abstract. The exact volume of brain tissue interrogated in near-infrared spectroscopy (NIRS) studies of cerebral oxygenation is unknown, the inhomogeneity of the head and resulting variation in optical paths making determination of the interrogated volume difficult. In this study, the spatial sensitivity profiles in simple two-component inhomogeneous cylindrical models are predicted by Monte Carlo simulation in order to reveal the effects of the overlying tissue on the volume of tissue interrogated by NIRS. The predictions are validated by experimental measurements on solid 'tissue equivalent' cylindrical phantoms. The phantom diameter is 30 mm and the thickness of the outer layer is 2 mm. The optical properties of the inner cylinder match those of adult brain white matter ($\mu'_{s1} = 6.4 \text{ mm}^{-1}$ and $\mu_{a1} = 0.02 \text{ mm}^{-1}$), but those of the outer layer are changed (μ'_{s0} from 1.7 to 8.3 mm^{-1} and μ_{a0} from 0.002 to 0.1 mm^{-1}). Results show that the spatial sensitivity profile is largely confined to the outer layer at small optode spacing ($< 15^\circ$) and to the inner layer at large spacing ($> 120^\circ$). At intermediate angles, the sensitivity profiles are sensitive to the optical properties of the outer layer. A low μ'_{s0} or μ_{a0} moves the profile toward the surface, at high μ_{a0} it moves in towards the inner layer and at high μ'_{s0} it is similar to the homogeneous case.

1. Introduction

Near-infrared spectroscopy (NIRS) which was first proposed in 1977 (Jöbsis 1977) is now widely used for cerebral oxygenation monitoring in adults (Ferrari *et al* 1986, Hazeki *et al* 1987, Hampson *et al* 1990, Hoshi and Tamura 1993), neonates (Wyatt *et al* 1986, Livera *et al* 1991, Edwards *et al* 1991) and fetuses (Aldrich *et al* 1994). The development of commercial instruments has enabled one to measure the oxygenation change in the brain routinely, via optical fibres attached to the head (Cope and Delpy 1988, Cope *et al* 1988, Chance *et al* 1990). One of the most important problems in interpretation of the NIRS data is to assess the volume of tissue in which the oxygenation change is being measured. It is obvious that the position and volume of the interrogated tissue will depend on the position and spacing of the source and detection fibres and this can roughly be estimated intuitively. For instance, since the mean interrogation depth of photons in a medium increases with increasing fibre spacing (Weiss *et al* 1989, Cui *et al* 1991), it is believed that oxygenation changes in the deeper tissues of the brain can be detected with large fibre spacing (Harris *et al* 1994). There is little rigorous evidence for this belief and most data are largely based on mathematical modelling and measurements in simple homogeneous phantoms (Patterson *et*

† JSPS Fellow for Research Abroad, original affiliation: Department of Electrical Engineering, Keio University, Yokohama, Japan.

al 1989, Jacques 1989). These give only ambiguous guidelines concerning the interrogated volume. Furthermore, in cerebral studies the overlying tissues, which consist of scalp, skull and cerebrospinal fluid around the brain, must affect the spatial sensitivity of the NIRS measurements. Some preliminary modelling of a simple two-layer model has shown that the photon propagation pathlength in the deeper layer (the 'brain') and also the reflected intensity at the surface are strongly affected by the optical properties of the overlying layer (the 'tissue') (Nossal *et al* 1988, Hiraoka *et al* 1993, Taitelbaum *et al* 1989, Cui and Ostrander 1992). However, the effect of the overlying tissue on the interrogated volume in the NIRS measurement has scarcely been investigated.

The volume of tissue interrogated with NIRS instrument can be obtained as the 'spatial sensitivity profile', which is deduced from the accumulated photon propagation path. There have been several publications on ways to estimate this parameter, many of which have been developed with the aim of NIR image reconstruction (Haselgrove *et al* 1991, Schotland *et al* 1993, Sevick *et al* 1994, Arridge 1995, Arridge and Schweiger 1995). These papers used various terms to describe the spatial sensitivity profiles, for instance photon hitting density (PHD) (Schotland *et al* 1993) or photon sampling volume (PSV) (Sevick *et al* 1994). In a previous series of studies, the term photon measurement density function (PMDF) (Arridge 1995, Arridge and Schweiger 1995) was proposed as the general description of the photon density path. The spatial sensitivity profile of the intensity measuring NIRS instruments is equivalent to the intensity PMDF.

In this study the effect on the spatial sensitivity profile of an inhomogeneity simulating the tissue overlying the brain is predicted in order to reveal the effect that this is likely to have on the volume of brain tissue interrogated with an NIRS instrument. To help elucidate these effects, a simplified cylindrical model was used which consists of two concentric homogeneous layers. A Monte Carlo method (Wilson and Adam 1983, van der Zee and Delpy 1987, Patterson *et al* 1990, Hasegawa *et al* 1991) is applied to the model to predict the spatial sensitivity profiles at various detection angles. In order to validate the Monte Carlo predictions, solid cylindrical 'tissue equivalent' phantoms (Firbank and Delpy 1993) have been built and 'mean time of flight' measurements of optical pathlength made at various detection angles using a pulsed laser system (Delpy *et al* 1988). The distortion of the spatial sensitivity profiles within the tissues caused by the outer layer and the consequent sensitivity of the NIR signals to changes in the inner 'brain' tissue are discussed.

2. The spatial sensitivity profile

In NIRS measurements one fibre is used for illumination and another detection fibre is placed nearby to collect the light passing through the tissue. The sensitivity profile, which shows the photon density distribution between the two fibres, namely the volume of tissue interrogated with the NIRS instrument, indicates the contribution of an attenuation change in a particular area to the total detected signal. The attenuation changes in biological tissues arise largely from variations in the haemoglobin concentration or oxygenation (Wray *et al* 1988). An intuitive description of the spatial sensitivity profile can be obtained in terms of the accumulated photon path histories reaching the detection fibre. In practice the histories of the photon paths are weighted by their output intensity and are recorded on a matrix for calculating the spatial sensitivity profile. The typical photon path of an individual photon and a weighted photon path history are shown in figure 1. A photon which has a unity weighting factor which is related to the intensity is put into the medium from a source fibre at r_0 . When the photon is scattered out from r_1 , where the detection fibre is located, the

spatial sensitivity of the photon at position (x, y) is defined as

$$E_i(x, y; \mathbf{r}_0, \mathbf{r}_1) = I_i(\mathbf{r}_0, \mathbf{r}_1)n \quad (1)$$

where x and y are discrete coordinates of the pixel, n is the number of passages of the photon through the pixel (x, y) and I_i is the output intensity of the i th photon. The spatial sensitivity profile is the accumulation of all the weighted path histories of the photons which reach \mathbf{r}_1 . The overall resultant spatial sensitivity at a pixel (x, y) can be obtained as the summation of the spatial sensitivity of all the photons:

$$E(x, y; \mathbf{r}_0, \mathbf{r}_1) = \sum_{i=0}^m E_i(x, y; \mathbf{r}_0, \mathbf{r}_1) \quad (2)$$

where m is the number of photons scattered out from \mathbf{r}_1 . The NIRS output is highly affected by absorption changes at the positions for which the values of the spatial sensitivity are greatest.

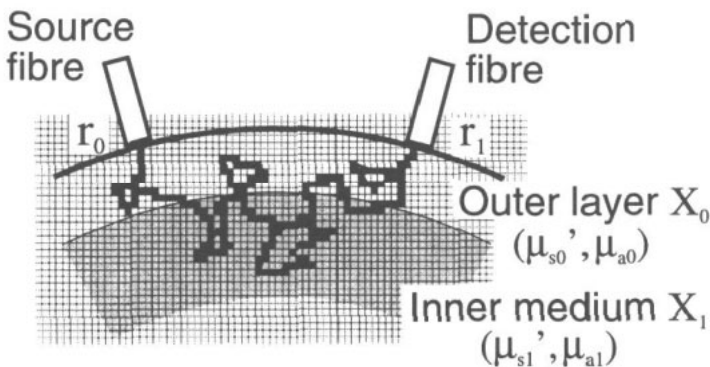


Figure 1. A typical photon path and weighted photon path history for calculating the spatial sensitivity profile.

Assume that an inhomogeneous medium consists of two separate homogeneous components which have different optical properties as shown in figure 1. The contribution of an absorption change in each component will depend upon the integrated spatial sensitivity summed over the component. In this study the outer layer X_0 and the inner medium X_1 imitate the overlying tissues of the head and the brain itself, respectively. Since the area of interest for NIRS measurement is the brain, we can define the sensitivity ratio $S(\mathbf{r}_0, \mathbf{r}_1)$, which is the spatial sensitivity summed over the inner medium X_1 divided by the spatial sensitivity summed over the whole area, to express the contribution of the brain to the total signal:

$$S(\mathbf{r}_0, \mathbf{r}_1) = \sum_{(x,y) \in X_1} E(x, y; \mathbf{r}_0, \mathbf{r}_1) / \sum_{(x,y) \in X_0, X_1} E(x, y; \mathbf{r}_0, \mathbf{r}_1). \quad (3)$$

The spatial sensitivity integrated over inner medium X_1 shows the fractional photon density in the inner medium and thus the sensitivity ratio indicates the contribution of the change in absorption in the inner medium to the NIRS output signal. Since the spatial sensitivity profile varies with the spacing between the source and the detection fibres, the sensitivity to the change in absorption in the inner medium relies not only on the optical properties of the media but also on the fibre spacing. A high value for the sensitivity ratio means that the output signal is dominated by absorption changes in the inner medium and indicates

that small changes in the optical properties of the outer layer can probably be ignored. Conversely, it would be hard to extract information about absorption changes in the inner medium from the NIRS signal under circumstances in which the sensitivity ratio is low.

3. The model and the method

3.1. The model

The geometry of the inhomogeneous model used in this study is shown in figure 2. The model consists of two homogeneous concentric cylinders. This simple geometry has been chosen for two reasons. Firstly, a previous theoretical study has shown that, when the input light is diffuse, the overall optical pathlengths are similar for the homogeneous slab, cylinder and sphere as a function of chord length (Arridge *et al* 1992). Secondly, for experimental verification of the data, it is much easier to make a multilayered cylindrical phantom. The outer diameter of the cylinder in the model is 30 mm and the thickness of the outer layer is 2 mm. Since the photon propagation in the model is predicted with a Monte Carlo simulation, the diameter of the model must be much smaller than that of the adult head to keep the computation time of the Monte Carlo simulation within reasonable limits. The ratio of the cylinder diameter and the thickness of the outer layer was, however, approximately equivalent to that of the adult brain diameter to the combined thickness of the scalp and skull. The model is a reasonable simulation of cerebral geometry in small animal models which are often used in NIR studies, for example rats (Delpy *et al* 1988, Wray *et al* 1988, Nomura and Tamura 1991), cats (Chance *et al* 1988), dogs (Ferrari *et al* 1989) and piglets (Tsuji *et al* 1995). The optical properties for the inner cylinder were transport scattering coefficient $\mu'_{s1} = 6.4 \text{ mm}^{-1}$ and absorption coefficient $\mu_{a1} = 0.02 \text{ mm}^{-1}$. These are almost equivalent to the optical properties of adult human and animal brain white matter (Cheong *et al* 1990). Four separate inhomogeneous models were used in which the optical properties of the outer layer were different from those of the inner cylinder. The differences of the optical properties of the outer layer were: (i) μ_{a0} the same, $\mu'_{s0} = 0.25 \mu'_{s1}$; (ii) μ_{a0} the same, $\mu'_{s0} = 1.3 \mu'_{s1}$; (iii) μ'_{s0} the same, $\mu_{a0} = 0.1 \mu_{a1}$; and (iv) μ'_{s0} the same, $\mu_{a0} = 5 \mu_{a1}$. A fifth homogeneous phantom whose outer layer optical properties were the same as those of the inner cylinder was also used for reference. The mean time of flight, output intensity and the spatial sensitivity profile were modelled as functions of the detection angle to examine the effect both of the optical properties of the outer layer and of the source-detection fibre spacing. In order to validate the Monte Carlo simulation, the predicted mean time of flight was compared with experimental results. The phantoms for these experiments were made of a clear polyester plastic containing titanium dioxide to alter its scattering coefficient and dyes to alter the absorption coefficient (Firbank and Delpy 1993). The refractive index of the polyester plastic is 1.58 and the mean cosine of the single-scattering phase function of the titanium dioxide was 0.58. The optical properties of the phantoms were the same as those of the corresponding models used in the simulation.

3.2. Monte Carlo simulation

A Monte Carlo simulation has the advantages of being conceptually simple and allowing direct handling of spatial sensitivity profiles because it predicts the propagation of individual photons. In this study the photon propagation was calculated using the variance reduction technique (Patterson *et al* 1990). Photons which have unit weight are injected into the model one-by-one at the position of the source fibre and the path of an individual photon is

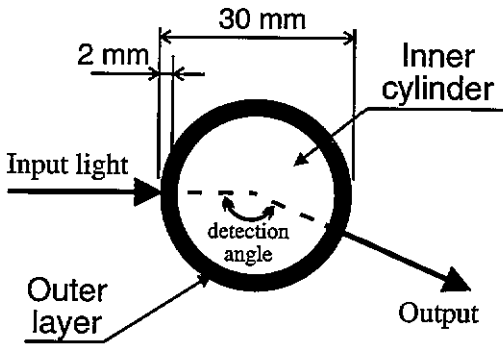


Figure 2. The geometry of the inhomogeneous model.

traced. The propagation of the photon in the model depends on the scattering coefficient, phase function and random numbers. The successive scattering lengths l_i are determined by

$$l_i = -\ln R/\mu_{si} \quad (4)$$

where μ_{si} is the scattering coefficient of medium i and R is a random number in the range 0–1. If a photon crosses the boundary between different media, then the scattering length is corrected. Successive scattering angles are calculated from random numbers and the scattering phase function. In order to compare the simulation results with experimental data, the experimentally measured scattering phase function of titanium dioxide was used in the calculation. Reflection and refraction of light on the surface of the model is taken into account. When the photon is scattered out of the model, the ultimate survival weight of the photon W is calculated from the absorption coefficients μ_{a0} , μ_{a1} and the accumulated pathlengths L_0 and L_1 in each medium:

$$W = W_0 \exp(-\mu_{a0}L_0 - \mu_{a1}L_1) \quad (5)$$

where W_0 is the survival weight of the photon, reduced only by reflection and refraction at the surface of the model.

It is assumed that the detection fibres with 5° aperture are located every 5° from 5° to 180° and that the values of $W|_\theta$ and $[W(L_0 + L_1)]|_\theta$ are recorded when the photon exits from the surface. If a photon arrives at a detection fibre at $\theta = 10^\circ, 30^\circ, 60^\circ$ or 150° , then the history of the photon path is accumulated into a matrix representing the spatial sensitivity profile for the detection fibre. After 5×10^6 photons have been traced the mean time of flight from the source fibre to each detection fibre is calculated as

$$\langle t(\theta) \rangle = \sum [W(L_0 + L_1)]|_\theta / \left(c \sum W|_\theta \right) \quad (6)$$

where c is the speed of light, corrected for the refractive index of the medium.

3.3. The experiment

A picosecond pulsed laser and a streak camera were used to measure the time of flight through the phantoms (Delpy *et al* 1988). The laser system consisted of an Ar-ion laser pumping a Ti:sapphire laser. Laser pulses of approximately 2 ps half-maximum width are emitted at 82 MHz. The laser was coupled into an optical fibre of 50 μm core diameter and guided to the phantom. A part of the laser beam is directly sampled as a delayed time

reference. The transmitted light at a particular detection angle θ is collected into a fibre bundle through a pinhole of 1 mm diameter and conveyed to the streak camera. The overall width of the pulse detected by the streak camera including fibre dispersion and jitter of the streak camera was 20 ps. The time of flight profile at various angles between source and detection fibres was measured and stored in a computer and the mean time of flight subsequently calculated after software corrections for non-linearity and so on in the streak camera.

4. Results

A comparison of the experimental results for the mean time of flight through the inhomogeneous and homogeneous phantoms with those predicted by the Monte Carlo simulation is shown in figure 3. Lines indicate the Monte Carlo predictions and symbols with error bars show the experimental results and the standard deviations of three measurements. The predicted mean time for each model agrees well with the experimental results except for the scatter in the Monte Carlo data at large detection angle because of poor statistics at large fibre spacing. The accuracy of the Monte Carlo calculation increases with the square root of the number of detected photons and, since the rate at which photons arrive at the fibre at large detection angles is extremely low, many millions of photons must be traced to obtain stable statistics. The mean times for the models which have a low μ'_{s0} or high μ_{a0} in the outer layer are shorter than that for the homogeneous model whereas for the models with high μ'_{s0} or low μ_{a0} outer layer, they are longer.

Images of the spatial sensitivity profiles of the homogeneous and inhomogeneous models for the detection angles of 10° , 30° , 60° and 150° are shown in figures 4–7, respectively. The white line shows the position of the boundary of the two layers. A hypothetical boundary is also shown in the spatial sensitivity profiles of the homogeneous model for reference. The bright parts of the images indicate high-sensitivity regions for the NIRS output signal and the contours in the image are drawn for every 12.5% fall from the maximum sensitivity point, with the extreme contour indicating the position where the relative sensitivity is 1%. Hence the contribution of optical property changes outside this final contour to the detected signal is almost negligible. As shown in figure 4, when the detection angle is 10° , because of the small fibre spacing, the interrogation depth is so shallow that the spatial sensitivity profiles are mainly distributed over the outer layer between the fibres and few photons pass through the inner cylinder. Hence the effect of object inhomogeneity on the profiles at small detection angle is not significant. The spatial sensitivity profiles for a detection angle of 30° are susceptible to the optical properties of the outer layer as shown in figure 5. In the homogeneous model the spatial sensitivity profile spreads uniformly between the fibres with the intense sensitivity area curved inward toward the centre and other sensitivity peaks located around the source and detection fibres. In the model with a low μ'_{s0} outer layer, the spatial sensitivity profile is obviously distorted in comparison with that of the homogeneous model. A localization of the intense sensitivity area along the boundary with the inner cylinder is observed in the image. The profiles of the models with the high μ'_{s0} or the low μ_{a0} outer layer are almost the same as that of the homogeneous model. The profile of the model with the low μ_{a0} is shifted slightly toward the cylinder surface and the overall spread of the profiles is less than that of the homogeneous model. In the model with the high μ_{a0} the sensitivity profile distribution is similar to that in the low μ'_{s0} model in that the peak of the intense region of sensitivity is observed at the boundary with the inner cylinder, yet the interrogation depth here is obviously the deepest of all the models. The spatial sensitivity profiles for the detection angle of 60° in figure 6 are of poorer quality and the contours show

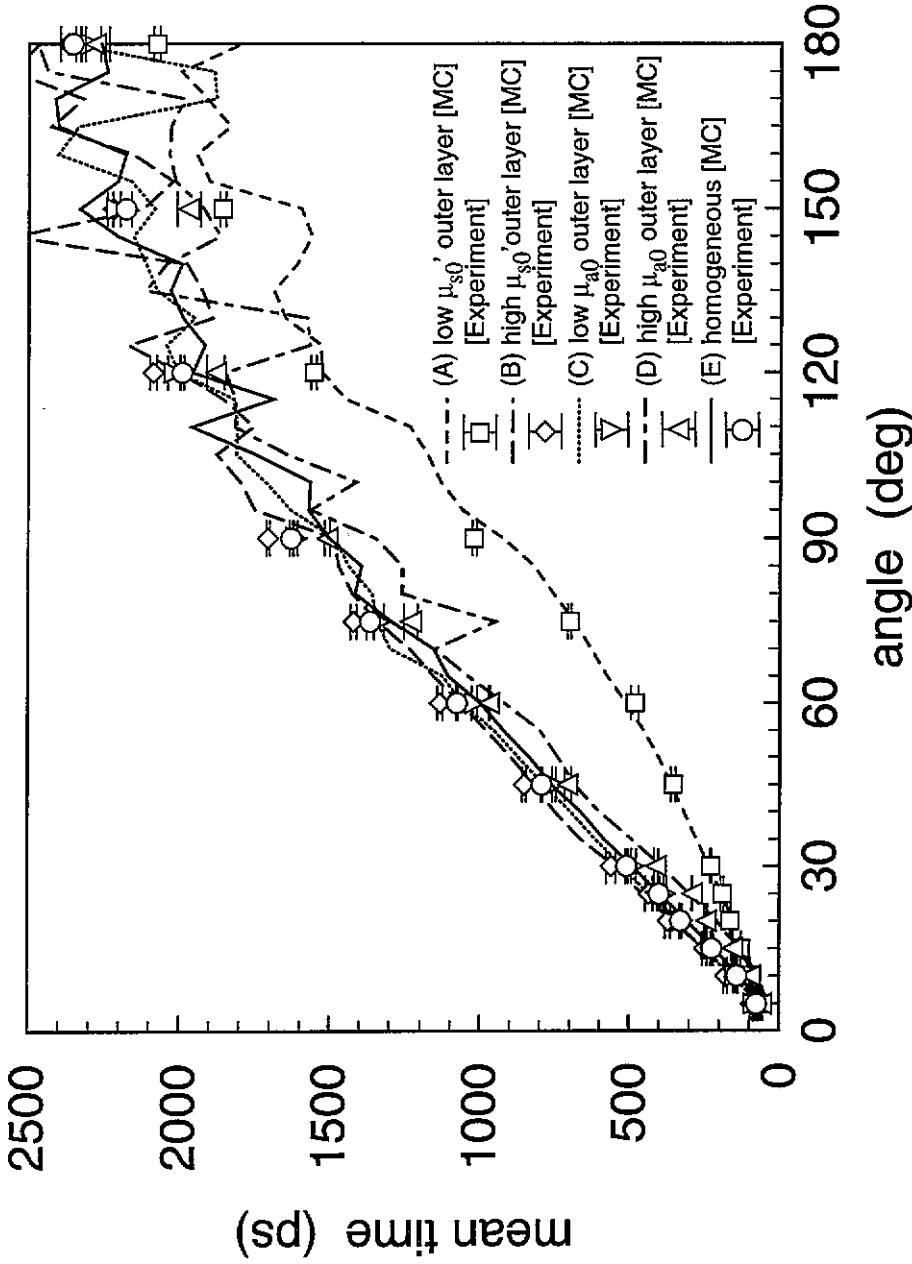


Figure 3. The mean time of flight estimated from Monte Carlo simulation compared with experimental results: (A) low μ_{s0}' outer layer (---, \square , $\pm 1SD$); (B) high μ_{s0}' outer layer (---, \diamond , $\pm 1SD$); (C) low μ_{a0} outer layer (....., ∇ , $\pm 1SD$) and (D) high μ_{a0} outer layer (---, Δ , $\pm 1SD$) and (E) homogeneous (—, \circ , $\pm 1SD$).

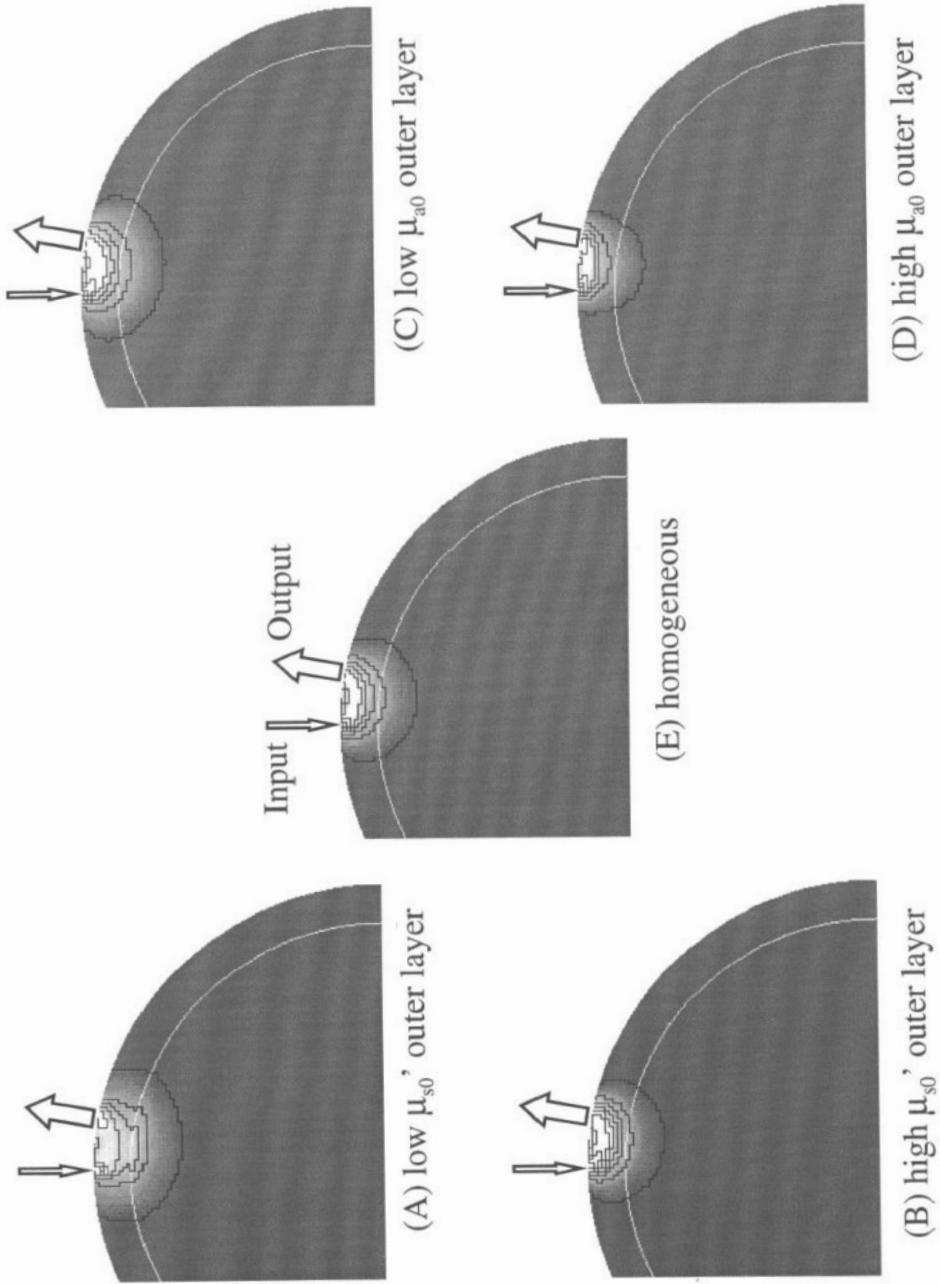


Figure 4. The spatial sensitivity profile at a detection angle of 10° .

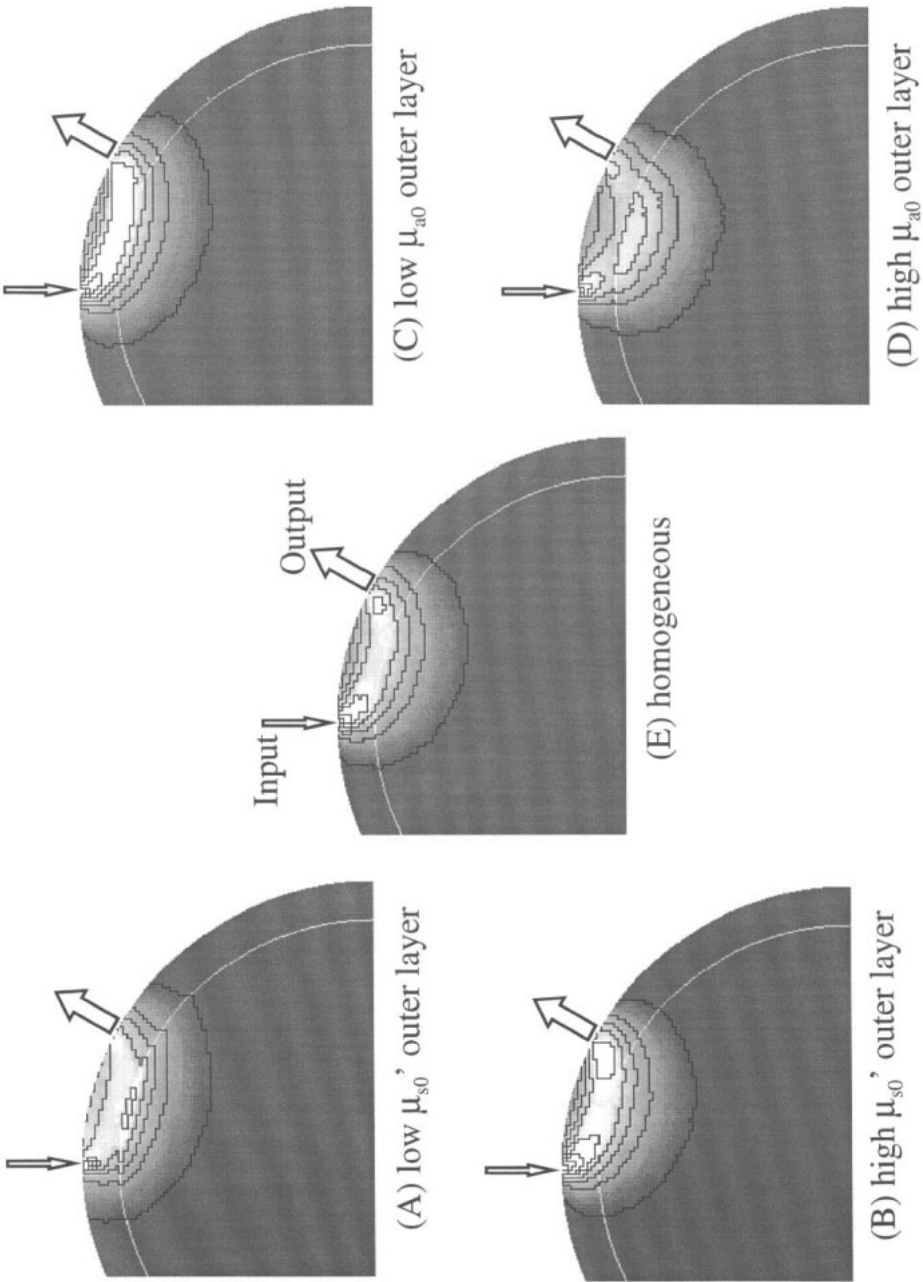


Figure 5. The spatial sensitivity profile at a detection angle of 30°

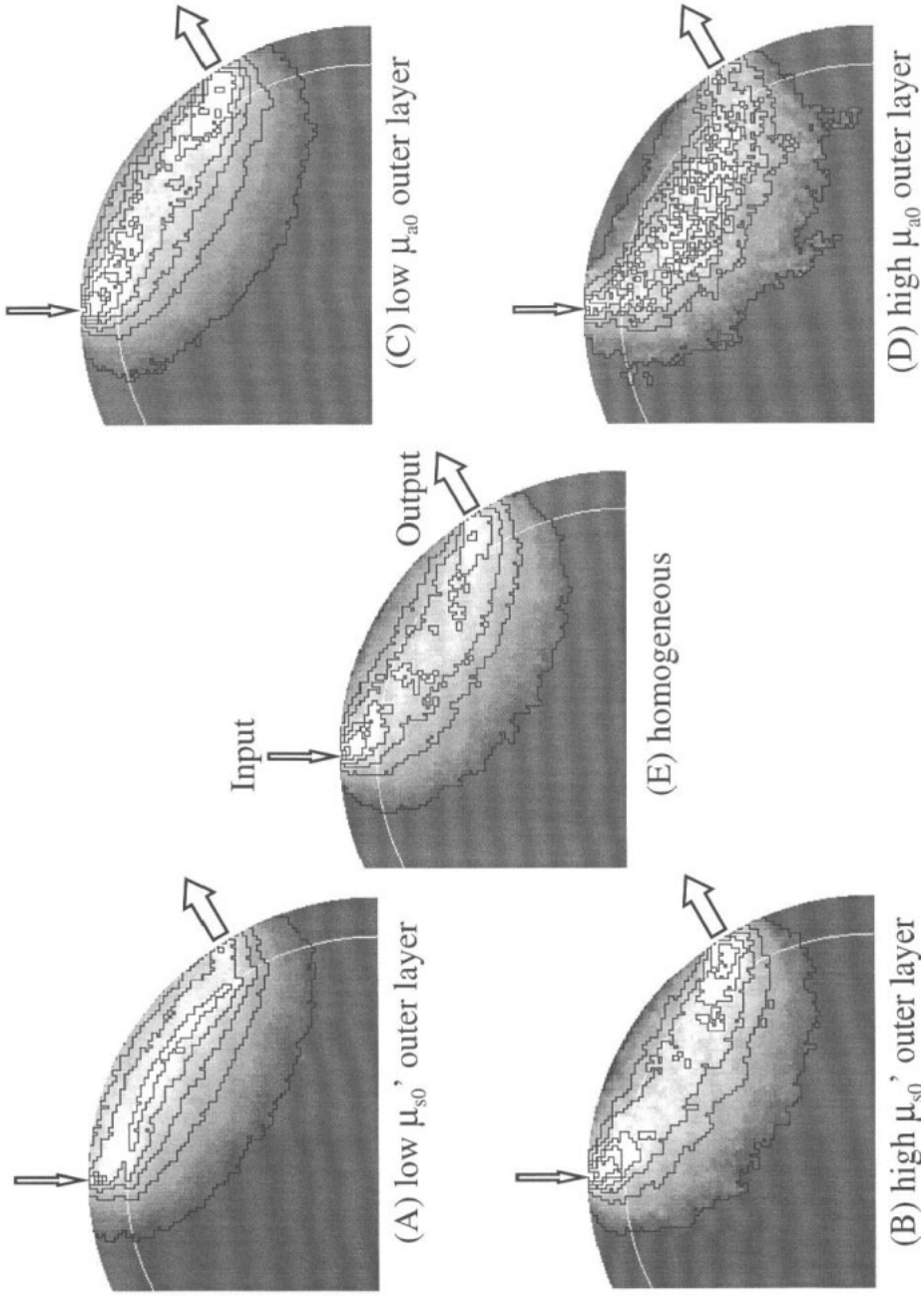


Figure 6. The spatial sensitivity profile at a detection angle of 60°

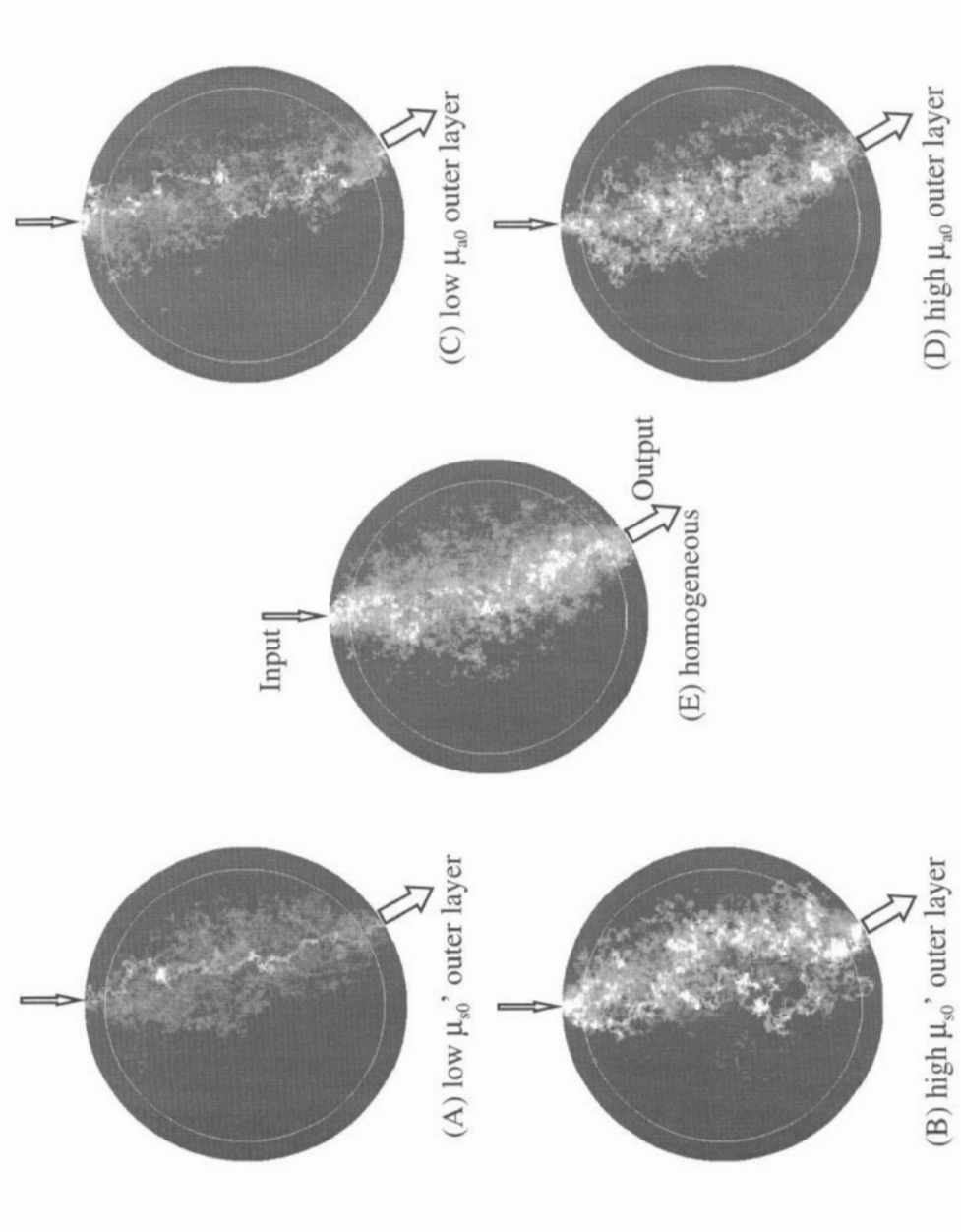


Figure 7. The spatial sensitivity profile at a detection angle of 150

the influence of noise, especially in the high μ_{a0} outer layer model. However, it can be seen that the tendencies of the profiles for each model are the same as those for a detection angle of 30° . For the detection angle of 150° shown in figure 7 the poor statistics of the Monte Carlo simulation make it impossible to provide a rigorous analysis of the sensitivity localization. However, it can be seen that there is a general tendency for the sensitivity profiles to stay close to the chord joining the source and detection fibre and there are few differences between the profiles of the models which have different optical properties in the outer layer.

Figure 8 shows the intensity of the output light on the surface of the inhomogeneous models as a function of the detection angle. The intensities are normalized with respect to those of the homogeneous model at each detection angle. The absolute magnitude of the intensity at over 90° is again uncertain because of the poor statistics. The surface intensities for the models which have a low μ'_{s0} or μ_{a0} outer layer are higher than those of the homogeneous model, whereas those for the high μ'_{s0} or μ_{a0} inhomogeneous models are lower.

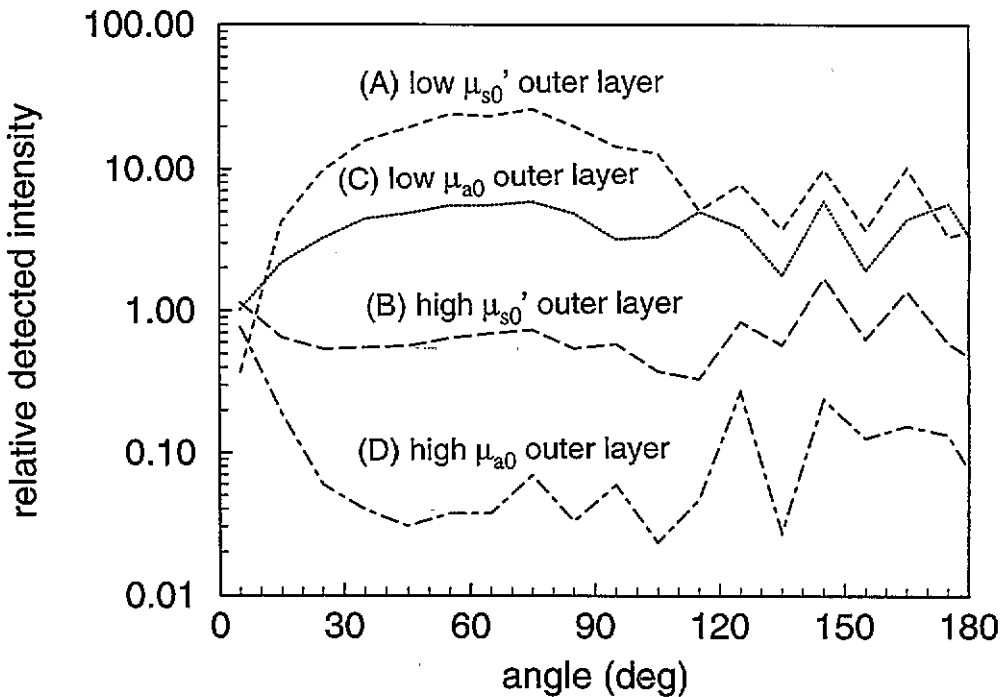


Figure 8. The relative detected intensity of each model predicted by Monte Carlo simulation as a function of angle.

The sensitivity ratio of the signal from the inner cylinder is shown in figure 9. The sensitivity ratios of each model at the small or large detection angles show little difference among themselves. At detection angles between 30° and 120° , a difference in the sensitivity ratio caused by the optical properties of the outer layer is, however, observed. The sensitivity ratio of the model with a high μ'_{s0} outer layer is almost the same as that of the homogeneous model. In the models with the low μ'_{s0} or low μ_{a0} outer layer, the sensitivity ratio is lower than that of the homogeneous model. However, in the model with the high μ_{a0} outer layer,

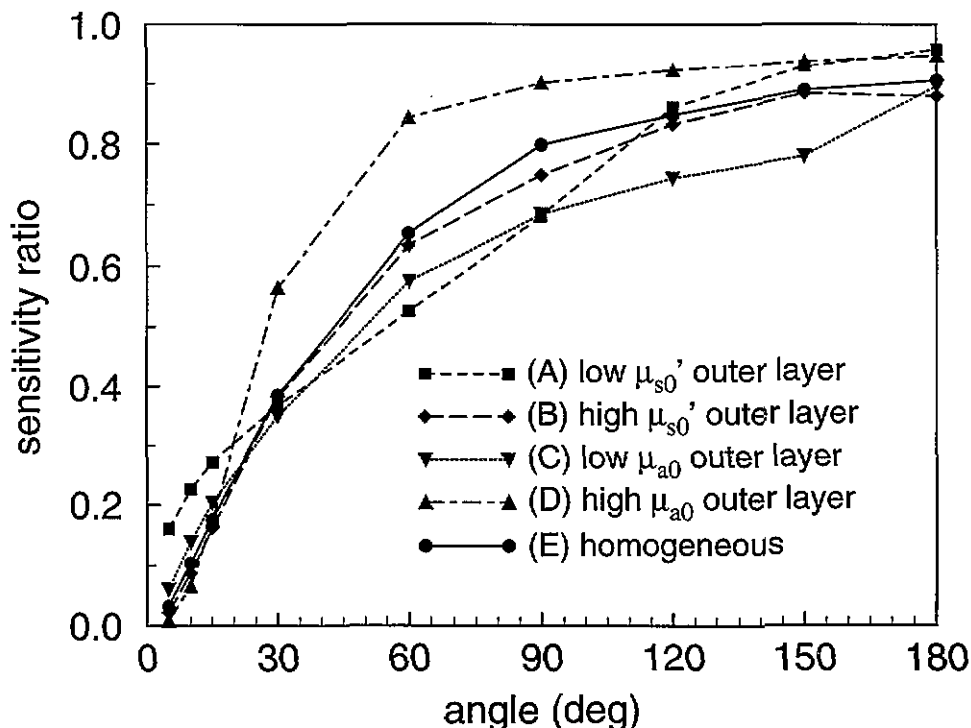


Figure 9. The effect of the optical properties of the outer layer on the sensitivity ratio.

the sensitivity ratio is much higher than that of the homogeneous model and it is over 0.8 at a detection angle of 60°.

5. Discussion

The spatial sensitivity profile in the homogeneous model forms the well-known curved 'banana' shape. The effects of the optical properties of the outer layer on the profile depend upon the detection angle. For small detection angles the profiles for the inhomogeneous models are mainly localized within the outer layer and have almost the same shape and curvature as that of the homogeneous model because of the shallow interrogation depth. On the other hand, at the larger detection angles, namely when the detection fibre is located almost opposite the source fibre, the spatial sensitivity profiles are distributed around the chord and little difference is caused by the optical properties of the outer layer. These results show that the spatial sensitivity profiles for the small detection angle are essentially determined by the optical properties of the outer layer, whereas the optical properties of the outer layer have very little effect on the spatial sensitivity profiles for the large detection angles and any NIRS instrument would detect the optical property changes along the chord in the inner medium. The sensitivity ratio confirms these results. The sensitivity ratio at the small detection angle is small; that is, a change in the output signal depends upon the optical property change in the outer layer but that at the large detection angles is almost independent of the optical property changes in the outer layer.

The differences between the spatial sensitivity profiles of each of the inhomogeneous

models are significant at intermediate angles. The profile distributions for models with a low μ'_{s0} outer layer and a high μ_{a0} outer layer are similar in that the significant-sensitivity area is localized upon the boundary in the inner cylinder. In the case of the model with the low μ'_{s0} outer layer, photons can easily reach the inner cylinder with few collisions and quite a few photons can also travel through the outer layer and on to the detector. Most of the detected photons which reach the inner cylinder only graze the inner cylinder's surface and the interrogation depth into the inner cylinder is shallow. As a consequence, the spatial sensitivity profile shifts toward the surface. Because of this, the sensitivity ratio of the low μ'_{s0} outer layer model is lower than that of the homogeneous model in spite of there being a higher overall detected intensity. It should be noted that the highest sensitivity region is still localized along the boundary and the interrogation depth hardly deepens when the detection angle increases to 60° . In the high μ_{a0} outer layer model, the photons which travel long pathlengths are highly attenuated and most of the photons which reach the detector take a detour into the inner cylinder whose μ_{a1} is lower. The spatial sensitivity in the outer layer is very low and the overall output intensity is much lower than that of the homogeneous model. Consequently the spatial sensitivity profile shifts toward the interior and the sensitivity ratio becomes higher. In the high μ'_{s0} outer layer model, photons are obstructed from reaching the inner cylinder or returning from there by the increased outer layer scattering. This causes slight reductions both in the relative detected intensity and in the sensitivity ratio. In the model with the lower μ_{a0} outer layer, photons which travel through the outer layer are attenuated less and the spatial sensitivity of the outer layer becomes relatively higher. Therefore the profile shifts towards the surface and the output intensity is higher than that of the homogeneous model.

Since the diameter of these models is considerably smaller even than that of the pre-term infant head and the degree of inhomogeneity is much less than in the real head, the results shown here cannot be applied directly to the interpretation of human cerebral NIRS data. Even though the ratio of the model diameter to the thickness of the outer layer was chosen to be almost equivalent to that of the brain diameter to the thickness of the scalp and skull, it is obvious that the absolute thickness of the outer layer is a considerable factor in determining the interrogated volume. If the outer layer is thicker than the interrogation depth of the photon, then the sensitivity profile at small fibre spacing is only dependent on the optical properties of the outer layer. Therefore a larger fibre spacing is needed to deliver photons to the inner cylinder when the diameter of the object is greater. It is relatively easy to visualize the features of the spatial sensitivity profile of the models at the small and large angles, but in practical use on the human adult, the NIRS fibre spacing is often 30° – 90° . These intermediate detection angles are those that are most susceptible to the optical properties of outer layer. In the adult head, the μ'_s of the scalp and skull is similar to that of grey matter and considerably lower than that of white matter. This suggests that the spatial sensitivity profile probably extends down to the boundary between grey and white matter and that the NIRS instrument mainly detects the oxygenation changes at the surface of the brain and in the grey matter. It is not possible to predict the photon propagation in a precise large model of the head using Monte Carlo simulation because of calculation time restrictions, but a finite-element method to solve the diffusion equation can also be used to predict the mean times of flight and photon-sensitivity profiles (Arridge *et al* 1993, Arridge and Schweiger 1995). Since the results of the finite-element method depend on several parameters, for example the mesh size, boundary condition and source condition, the implementation of the diffusion equation in the finite-element method is more complicated than the Monte Carlo calculation. However, it has the advantage of fast calculation time and it is probably the most effective technique to predict the photon propagation in large complicated models.

6. Conclusions

A Monte Carlo investigation was carried out to reveal the effects of the optical properties in the outer layer on the volume of tissue interrogated by NIRS instruments. The results comparing the mean times of flight of the Monte Carlo prediction with experimental measurements using a pulsed laser system showed the validity of the prediction. The features of the spatial sensitivity profile as a function of the detection angle can be summarized into three categories: (i) at small detection angles the profile is localized within the outer layer only, (ii) at intermediate detection angles the NIRS signal contains information about changes in the optical properties of the inner cylinder but its sensitivity and the localization of the sensitive region are highly affected by the optical properties of outer layer and (iii) at large detection angles the profile depends mainly on the optical properties of the inner cylinder. Since NIRS measurement of the human head are made mainly at intermediate angles, it is important to examine the optical properties of the outer layer in order to determine the interrogated region.

Acknowledgments

This work was supported by a Japan Society for the Promotion of Science Postdoctoral Fellowship for Research Abroad to Eiji Okada, and funding from the EPSRC (grant GR/K07386), the Wellcome Trust and Hamamatsu Photonics KK.

References

- Aldrich C J, Wyatt J S, Spencer J A, Reynolds E O R and Delpy D T 1994 The effect of maternal oxygen administration of human fetal cerebral oxygenation measured during labour by near infrared spectroscopy *Br. J. Obstet. Gynaecol.* **101** 509–13
- Arridge S R 1995 Photon measurement density functions: part I. Analytical forms *Appl. Opt.* at press
- Arridge S R, Cope M and Delpy D T 1992 The theoretical basis for the determination of optical pathlength in tissue: temporal and frequency analysis *Phys. Med. Biol.* **37** 1531–60
- Arridge S R and Schweiger M 1995 Photon measurement density functions, part II. Finite element method calculations *Appl. Opt.* at press
- Arridge S R, Schweiger M, Hiraoka M and Delpy D T 1993 A finite element approach for modelling photon transport in tissue *Med. Phys.* **20** 299–309
- Chance B *et al* 1988 Comparison of time-resolved and un-resolved measurement of deoxy hemoglobin in brain *Proc. Natl Acad. Sci. USA* **85** 4971–5
- Chance B, Maris M, Sorge J and Zhang M Z 1990 A phase modulation system for dual wavelength difference spectroscopy of haemoglobin deoxygenation in tissue *Proc. SPIE* **1204** 481–91
- Cheong W F, Prah S A and Welch A J 1990 A review of the optical properties of biological tissues *IEEE J. Quant. Electron.* **26** 2166–85
- Cope M and Delpy D T 1988 System for long term measurement of cerebral blood and tissue oxygenation on newborn infants by near infrared transillumination *Med. Biol. Eng. Comput.* **26** 289–94
- Cope M, Delpy D T, Reynolds E O R, Wray S, Wyatt J and van der Zee P 1988 Methods of quantitating cerebral near infrared spectroscopy data *Adv. Exp. Med. Biol.* **222** 183–9
- Cui W, Kumar C and Chance B 1991 Experimental study of migration depth for the photons measured at sample surface *Proc. SPIE* **1431** 180–91
- Cui W and Ostrander L E 1992 The relationship of surface reflectance measurements to optical properties of layered biological media *IEEE Trans. Biomed. Eng.* **39** 194–201
- Delpy D T, Cope M, van der Zee P, Arridge S R, Wray S and Watt J S 1988 Estimation of optical pathlength through tissue from direct time of flight measurement *Phys. Med. Biol.* **33** 1433–42
- Edwards A D, Brown G C, Cope M, Wyatt J S, McCormick D C, Roth S C, Delpy D T and Reynolds E O R 1991 Quantification of concentration changes in neonatal human cerebral oxidized cytochrome oxidase *J. Appl. Phys.* **71** 1907–13

- Ferrari M, Wilson D A, Hanley D F, Hartmann J F, Rogers M C and Traystman R J 1989 Noninvasive determination of hemoglobin saturation in dogs by derivative near-infrared spectroscopy *Am. J. Physiol.* **256** H1493-9
- Ferrari M, Zanette E, Giannini I, Sideri G, Fieschi C and Carpi A 1986 Effect of carotid artery compression test on regional cerebral blood volume, haemoglobin oxygen saturation and cytochrome-c-oxidase redox level in cerebrovascular patients *Adv. Exp. Med. Biol.* **200** 213-22
- Firbank M and Delpy D T 1993 A design for a stable and reproducible phantom for use in near infra-red imaging and spectroscopy *Phys. Med. Biol.* **38** 847-53
- Hampson N B, Camporesi E M, Stolp B W, Moon R E, Shook J E, Griebel J A and Piantadosi C A 1990 Cerebral oxygen availability by NIR spectroscopy during transient hypoxia in humans *J. Appl. Phys.* **69** 907-3
- Harris D N F, Cowans F M, Wertheim D A and Hamid S 1994 NIRS in adults—effect of increasing optode separation *Adv. Exp. Med. Biol.* **345** 837-40
- Hasegawa Y, Yamada Y, Tamura M and Nomura Y 1991 Monte Carlo simulation of light transmission through living tissues *Appl. Opt.* **30** 4515-20
- Haselgrove J, Leigh J, Yee C, Wang N, Maris M and Chance B 1991 Monte Carlo and diffusion calculations of photon migration in non-infinite highly scattering medium *Proc. SPIE* **1431** 30-41
- Hazeki O, Seyama A and Tamura M 1987 Near infrared spectrophotometric monitoring of haemoglobin and cytochrome aa₃ *in vivo* *Adv. Exp. Med. Biol.* **215** 283-9
- Hiraoka M, Firbank M, Essenpreis E, Cope M, Arridge S R, van der Zee P and Delpy D T 1993 A Monte Carlo investigation of optical pathlength in inhomogeneous tissue and its application to near-infrared spectroscopy *Phys. Med. Biol.* **38** 1859-76
- Hoshi Y and Tamura M 1993 Detection of dynamic changes in cerebral oxygenation coupled to neuronal function during mental work in man *Neurosci. Lett.* **150** 5-8
- Jacques S L 1989 Time-resolved reflectance spectroscopy in turbid tissues *IEEE Trans. Biomed. Eng.* **36** 1155-61
- Jöbsis F F 1977 Non invasive, infrared monitoring of cerebral and myocardial oxygen sufficiency and circulatory parameters *Science* **198** 1264-7
- Livera L N, Spencer S A, Thorniley M S, Wickramasinghe Y A B D and Rolfe P 1991 Effects of hypoxemia and bradycardia on neonatal cerebral haemodynamics *Arch. Dis. Childhood* **66** 376-80
- Nomura Y and Tamura M 1991 Quantitative analysis of hemoglobin oxygenation state of rat brain *in vivo* by picosecond time-resolved spectrophotometry *J. Biochem.* **109** 455-61
- Nossal R, Kiefer J, Weiss G H, Bonner R, Taitelbaum H and Havlin S 1988 Photon migration in layered media *Appl. Opt.* **27** 3382-91
- Patterson M S, Chance B and Wilson B C 1989 Time resolved reflectance and transmittance for the non-invasive measurement of tissue optical properties *Appl. Opt.* **28** 2331-6
- Patterson M S, Wilson B C and Wyman D 1990 The propagation of optical radiation in tissue I. Models of radiation transport and their application *Lasers Med. Sci.* **6** 155-68
- Schotland J C, Haselgrove J C and Leigh J S 1993 Photon hitting density *Appl. Opt.* **3** 448-53
- Sevick E M, Burch C L, Frisoli J K and Lakowicz J R 1994 Localization of absorbers in scattering media by use of frequency-domain measurements of time-dependent photon migration *Appl. Opt.* **33** 3562-71
- Taitelbaum H, Havlin S and Weiss G H 1989 Approximate theory of photon migration in a two-layer medium *Appl. Opt.* **28** 2245-9
- Tsuji M, Haruse H, Volpe J and Holtzman D 1995 Reduction of cytochrome aa₃ measured by near-infrared spectroscopy predicts cerebral energy loss in hypoxic piglets *Pediatr. Res.* **37** 253-9
- van der Zee P and Delpy D T 1987 Simulation of the point spread function for light in tissue by a Monte Carlo technique *Adv. Exp. Med. Biol.* **215** 179-91
- Weiss G H, Nossal R and R F Bonner 1989 Statistics of penetration depth of photons re-emitted from irradiated tissue *J. Mod. Opt.* **36** 349-59
- Wilson B C and Adam G 1983 A Monte Carlo model for the absorption and flux distributions of light in tissue *Med. Phys.* **10** 824-30
- Wray S, Cope M, Delpy D T, Wyatt J S and Reynolds E O R 1988 Characterization of the near-infrared absorption spectra of cytochrome aa₃ and hemoglobin for a non-invasive monitoring of cerebral oxygenation *Biochem. Biophys. Acta* **993** 184-92
- Wyatt J S, Delpy D T, Cope M, Wray S and Reynolds E O R 1986 Quantification of cerebral oxygenation and haemodynamics in sick newborn infants by near infrared spectrophotometry *Lancet* **2** 1063-6